Computers in Biology and Medicine 111 (2019) 103343

Contents lists available at ScienceDirect

Computers in Biology and Medicine

journal homepage: www.elsevier.com/locate/compbiomed

Estimation of mechanical parameters in cancers by empirical orthogonal function analysis of poroelastography data

Md Tauhidul Islam, Raffaella Righetti*

Department of Electrical and Computer Engineering, Texas A&M University, College Station, TX, 77840, USA

ARTICLE INFO

Keywords:
Elastography
Poroelastography
Cancer imaging
Young's modulus
Poisson's ratio
Vascular permeability

ABSTRACT

Ultrasound poroelastography is a non-invasive imaging modality that has been shown to be capable of estimating mechanical parameters such as Young's modulus (YM), Poisson's ratio (PR) and vascular permeability (VP) in cancers. However, experimental poroelastographic data are inherently noisy because of the requirement of relatively long temporal data acquisitions often in hand-held mode conditions. In this paper, we propose a new method, which allows accurate estimation of YM and PR from denoised steady state axial and lateral strains by empirical orthogonal function (EOF) analysis of poroelastographic data. The method also allows estimation of VP from the time constant (TC) of the first expansion coefficient (EC) of the temporal axial strain, which has larger dynamic range and lower noise in comparison to the actual temporal axial strain curve. We validated our technique through finite element (FE) and ultrasound simulations and tested the in vivo feasibility in experimental data obtained from a cancer animal model. The percent relative errors (PRE) in the estimation of YM, PR and VP using the EOF analysis as applied to ultrasound simulation data were 3.27%, 3.10%, 14.22%, respectively (at SNR of 20 dB). Based on the high level of accuracy by EOF analysis, the proposed technique may become a useful signal processing technique for applications focusing on the estimation of the mechanical behavior of cancers.

1. Introduction

The mechanical properties of cancers have a profound effect on cancer development and metastasis and affect effectiveness of cancer treatments [29,38]. The Young's modulus (YM) is a mechanical parameter, which is defined as the ratio of the applied axial stress and associated induced local axial strain in elastic solid materials [12] and provides an indication of the stiffness of a tumor [50]. The Poisson's ratio (PR) is related to the compressibility of tissues. It is defined as the ratio of lateral strain to axial strain in a homogeneous material. In inhomogeneous materials, the PR is related to the lateral to axial strain ratio in a more complex manner [12]. Vascular permeability (VP) is related to the compliance of fluid flow inside a poroelastic material and is defined as the discharge of fluid per unit area between two points having a unit pressure difference. The aforementioned parameters have been shown to be of great clinical significance for the assessment of cancers and related treatments. To date, there are only a few modalities that can be used to image these parameters in vivo. YM can be imaged by non-invasive imaging modalities, which include: ultrasound elastography [42], ultrasound shear wave elastography [47] and magnetic resonance elastography [36]. VP has been assessed using MRI-based [8,11] and optical-based [34] methods. Recent work from our laboratory has demonstrated the feasibility of non-invasively imaging YM, PR and VP using ultrasound poroelastography [27,28].

Ultrasound poroelastography is a technique that aims at imaging the mechanical behavior of tissues related to fluid transport mechanisms [43,44]. In poroelastography, the time dependent strains induced in a tissue subjected to sustained compression are estimated and analyzed. As the poroelastic material in steady state behaves as a linear elastic solid, it is possible to estimate YM and PR from the strains in steady state conditions. Additionally, the temporal behavior of the axial and lateral strains is related to the VP and interstitial permeability (IP) of the tissue, and this connection allows us to measure these parameters from the analysis of the temporal strains [23,24].

In previous works, we have provided and tested methods to estimate YM, PR and VP in tumors in a mouse animal model by using axial and lateral strain elastograms obtained during a poroelastography experiment [27,28]. In Ref. [27], we proposed a method to estimate YM and PR in tumors of different shape. This method was then extended to tumors with irregular boundaries [28]. Additionally, in Ref. [28], we demonstrated that estimation of VP in regular/irregular shaped tumors is possible by measuring the axial strain TC induced in a tissue during a

* Corresponding author.
E-mail address: righetti@ece.tamu.edu (R. Righetti).

https://doi.org/10.1016/j.compbiomed.2019.103343
Received 5 December 2018; Received in revised form 24 May 2019; Accepted 24 June 2019

poroelastography experiment. Methods proposed for estimation of axial strain TC are mostly curve-fitting based [37]. However, estimation of parameters from data by fitting a non-linear exponential function is challenging because small changes in the data due to noise or incorrect measurements can change the estimated parameter drastically [14]. In addition, experimental strain data in vivo are noisy as poroelastography experiments require prolonged data acquisitions oftentimes in free-hand mode (at least one minute [27], and the quality of lateral strain estimation, which is important in parameter reconstruction using poroelastography [27], is limited. The noise affecting the acquired strain data in practical poroelastography experiments can create a large number of local minima in the cost function of the strain TC estimator increasing significantly the number of computations to find the global minimum.

To denoise axial and lateral strains, several methods have been proposed in the literature. Kalman filtering has been used in a number of studies to remove noise from axial and lateral strains [17,21,32,45]. Geometric diffusion filtering has been proposed in Ref. [18] to denoise the axial strains. Recently, we have proposed a filtering technique based on a combination of Kalman and non-linear complex diffusion filters, which has been shown to be very effective in removing noise from the strains in fluid pressure estimation using poroelastography [25]. However, most of these techniques are effective in removing noise affecting the spatial distribution of the strains but less effective in removing noise affecting their temporal distribution. Additionally, the common problem of all these techniques is that improvement of SNR is achieved at the expenses of spatial resolution. The amount of lost spatial resolution depends on the signal power of the filter, and this is difficult to optimize in available techniques. EOF analysis has been explored in Tyagi et al. [49] to denoise strains obtained from noisy ultrasonic data while optimizing SNR improvement and spatial resolution reduction. However, this method was limited to the estimation of spatial variations and is not applicable to poroelastography, where the strains are time dependent, and estimation of both temporal and spatial variations is necessary. In Ref. [9], EOF analysis was used to improve estimation of the spatial distribution of elastographic strains. This method does not allow estimation of any temporal characteristics of the strains, rather it is used similarly to temporal averaging to improve image quality. In Ref. [33], EOF analysis was used for automated classification of tissue response to acoustic radiation force impulse excitation.

In this paper, we propose the use of empirical orthogonal function (EOF) analysis to denoise the axial and lateral strains obtained from poroelastography experiments. EOF analysis is a popular method for dimensionality reduction and determination of spatio-temporal patterns in a data set [13,15,39]. EOF analysis works to find a new set of variables that can capture most of the observed variance of the data through a linear combination of the original variables. The EOF analysis is designed for analyzing the variability of a single field, i.e., a field of only one scalar variable (axial or lateral strain, in our case). The method finds the spatial patterns of variability, their time variation and gives a measure of the importance of each pattern.

EOF analysis is in essence a non-model based exploratory tool, which is able to produce a time display and a space display of the space-time field of a parameter of interest [4]. Thus, EOF analysis can be particularly useful in poroelastography applications, where the space-time behavior of the strains is of fundamental importance for the determination of the tissue mechanical parameters. More specifically, EOF analysis can be used to obtain the display of temporal and spatial patterns of the strain variables with reduced noise. This allows us to reconstruct the YM and PR from the denoised strain data based on the first EC from EOF analysis only and used curve fitting technique on the first EC to obtain the axial strain TC, which is needed to estimate the VP. Our proposed method differs substantially from aforementioned methods that used EOF in the context of strain imaging because our analysis aims at estimating both the spatial and temporal distributions of the strains to obtain different tissue mechanical properties.

Abbreviations used in this paperare given in Table 1.

Table 1
Abbreviation.

Term	Abbreviation	Term	Abbreviation
Young's modulus	YM	Poisson's ratio	PR
Vascular permeability	VP	Interstitial permeability	IP
Time constant	TC	Empirical orthogonal function	EOF
Expansion coefficient	EC	Finite element	FE
Percent relative error	PRE	Radio frequency	RF
Signal to noise ratio	SNR	Mega hertz	MHz

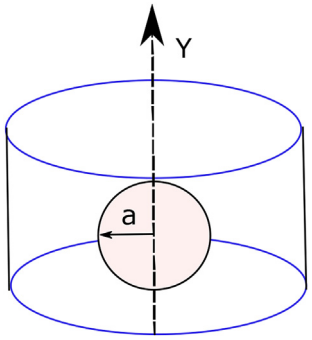

Fig. 1. A schematic of a cylindrical sample of a poroelastic material with a spherical inclusion of radius *a*. The axial direction is along the *y*-axis.

2. Problem formulation

The schematic of a poroelastic sample under creep compression in a poroelastography experiment is shown in Fig. 1. Although the inclusion and sample can be of various shapes, we show a cylindrical sample with spherical inclusion. We use this sample for the simulations because, in most works in the literature, the tumor is reported or assumed to be of spherical shape [1,38] and because the cylindrical shape assumption for the sample is frequently used in elastography due to the way the sample is compressed [22].

The equations for axial, lateral and volumetric strains in a poroelastic material depend on the geometry and boundary conditions and contain an infinite number of exponentials. However, in a recent study from our group [20], we have proved that the contribution of the first exponential is dominant, and a negligible amount of error is introduced in the analysis of the behavior of a poroelastic material if higher order exponentials are not considered. In another work [19], we have developed a common model for strains in poroelastic materials of different geometry, boundary conditions and experimental protocol. In Ref. [19], the equation for axial strain is developed as follows:

$$s(t) = \eta + \gamma e^{-\frac{t}{\tau}}, \tag{1}$$

where $s(t)$ is the axial strain temporal curve, η is the value of s at steady state (i.e., at $t = \infty$) and γ is a constant parameter, which differs based on material properties and experimental protocol. Eq. (1) is applicable for axial strain in a poroelastic sample irrespective of shape of the sample and the inclusion. Assuming the microfiltration coefficient $\chi \gg \frac{k}{a^2}$, where k is the interstitial permeability (IP) and a is fluid path, we can write for axial strain TC

$$\tau = \frac{1}{H_A \chi}. \tag{2}$$

Here, aggregate modulus, $H_A = \frac{E(1-\nu)}{(1-2\nu)(1+\nu)}$ and $\chi = L_p \frac{S}{V}$ [23,24]. E and ν are the YM and PR of the poroelastic sample. L_p and $\frac{S}{V}$ are the VP and surface are to volume ratio of capillary walls inside the sample. Eq. (2)

is applicable for axial strain TC in both the inclusion and background irrespective of shape of the inclusion, when the assumption $\chi \gg \frac{k}{a^2}$ is satisfied. The condition $\chi \gg k/a^2$ implies that VP is dominant over the IP. As the capillary vessels are distributed throughout the tumors, the fluid flow and fluid pressure are the same everywhere, and the strains and fluid pressure are spatially invariant inside the tumors. The strain TC becomes function of only the VP for this case. However, if IP is dominant or comparable to VP, fluid flow and pressure distribution are spatially variant inside the tumor. In this case, the strain TC depends on the VP as well as the IP of the tumors [23,26].

To estimate VP inside the poroelastic sample, axial strain TC, YM and PR need to be estimated. The techniques for estimation of these parameters along with the EOF analysis of axial and lateral strain data to remove noise from the strains are discussed in the next sections.

3. Empirical orthogonal function analysis

3.1. Theory

The aim of EOF analysis is to find uncorrelated linear combinations of a number of variables and their importance in variability of data by finding the decomposition of a continuous space-time data field $S(t, \boldsymbol{x})$, where t and $\boldsymbol{x}$ denote time and spatial positions, respectively [13,15,39]. To achieve this goal, the first EOF accounts for the highest variance in the data and each succeeding EOF has the largest possible variance under the constraint that it is orthogonal to all former EOFs. As a result, the computed EOFs become members of an uncorrelated orthogonal basis set. Therefore, through EOF analysis, we have to find a vector $\boldsymbol{E} = (E_1,...,E_p)^T$ such that the columns of $S\boldsymbol{E}$ contain descending variability and the E_i s are orthogonal to each other. This problem can be written as an optimization problem as

$$\underset{E_i}{\text{argmax}} \sum_{j=1}^{p} (E_i d_j)^2, \tag{3}$$

where, d_j is j^{th} column of D, which is the matrix obtained after removal of the time mean from the data matrix S containing poroelastic strains (see Fig. 2). We refer to Ref. [4] for details on the process of removal of the time mean from the matrix S. Additionally, the orthonormality condition should be satisfied on E_i while solving eq. (3):

$$E_i^T E_j = \delta_{ij}, \tag{4}$$

where superscript T denotes the transpose operation. We notice that

$$\sum_{j=1}^{p} (E_i d_j)^2 = E_i D^T D E_i^T = E_i R E_i^T. \tag{5}$$

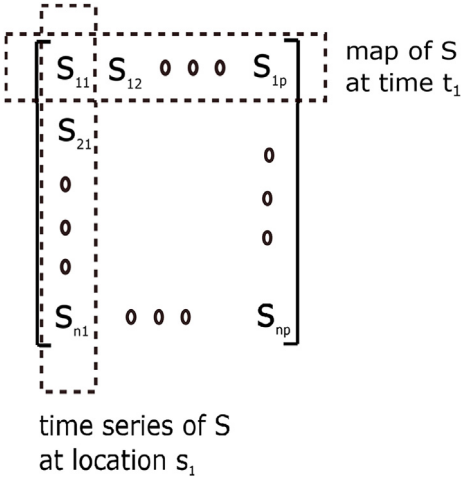

Fig. 2. Data structure of poroelastic strains for EOF analysis.

The maximization of eq. (3) subject to eq. (4) gives

$$\nabla(u^T R u) - \lambda \nabla(u^T u) = 0, \tag{6}$$

where u is the optimization variable, ∇ is the gradient operator and λ is a Lagrange multiplier. Further simplification of eq. (6) results in

$$Ru = \lambda u. \tag{7}$$

This equation can also be written as

$$RC = C\Lambda, \tag{8}$$

where Λ is a diagonal matrix containing the eigenvalues λ_i, $i = 1, ...,n$ of R. The column vectors of C are the eigenvectors of R, E_i corresponding to the eigenvalues λ_i.

If we construct a matrix A with the ECs a_i, $i = 1, ...,n$, A can be determined as

$$A = DC. \tag{9}$$

We can also reconstruct the original data from the EOFs and the ECs using following formula

$$D = \sum_{i=1}^{n} a_i(t) E_i(\boldsymbol{x}). \tag{10}$$

Noisy signal matrix S can be reconstructed using D and time mean subtracted from S. However, the first few EOFs carry more information about the signal than noise and successive EOFs carry more information about noise than the signal. Therefore, a common technique in many signal analysis paradigms is to first use few EOFs, i.e., $i = q < n$ to obtain a cleaner version of the original noisy signal.

3.2. Data process

Axial and lateral strain data are represented as arrays containing 2D data at each time point. Therefore, the axial/lateral strain data F is a function of time x, y and t. We suppose that the horizontal coordinates of F are discretized to yield x_j, $j = 1, ...,p_1$, and y_k, $k = 1, ...,p_2$, and similarly for time, i.e. t_i, $i = 1, ...,n$. The discretized field reads:

$$F_{ijk} = F(x_j, y_k, t_i). \tag{11}$$

with $1 \le i \le n$, $1 \le j \le p_1$, and $1 \le k \le p_2$. It is in general tedious and memory consuming to process three-dimensional arrays such as F. We therefore transform F into a two-dimensional array: the data matrix S, where the two spatial dimensions are concatenated together. We suppose that we have a gridded data set composed of a space-time field $S(t_i, s_j)$ representing the value of the field F at time t_i and spatial position (x_j, y_k). The value of the field at discrete time t_i and grid point s_j is denoted by S_{ij} for $i = 1, ...,n$ and $j = 1, ...,p = p_1 p_2$. The data structure for EOF analysis of poroelastic strains is shown in Fig. 2.

The EOF analysis algorithm along with data structure formation is described in Box 1.

4. Determination of YM, PR and VP

To determine the YM, PR and VP of the tumor (inclusion) and background tissue, we use the theories developed in Refs. [27,28]. In brief, the YM and PR of the tumor are estimated using a cost function minimization technique developed from Eshebly's inclusion theory [12,35]. The cost function is the squared value of the difference between two expressions of the same eigen function inside the inclusion developed in Eshelby and Mura's work [12]. One expression of the eigen function incorporates the YM and PR of both the tumor and normal tissue, and the other incorporates only the PR of normal tissue. Both expressions use the axial and lateral strains at steady state from the poroelastography experiment. If the tumor is of any other shape than ellipse or sphere, its shape is approximated by an ellipse [27,28].

Eq. (1) is fit onto the first EC of the axial strain by curve fitting technique to estimate the axial strain TC τ [37]. The VP of tumors/

Box 1
Algorithm for EOF analysis of poroelastic data

1. Form 2D data matrix S by concatenating the two spatial coordinates from poroelastic strain data F, which is three-dimensional (2D axial/lateral strain at each time point).
2. Remove the mean value from each column of the data matrix S to obtain matrix D.
3. Find the covariance matrix $R = D^T D$.
4. Find the eigenvalues and eigenvectors of R by solving $RC = C\Lambda$.
5. Find the biggest eigenvalues and their corresponding eigen vectors (EOFs).
6. Find the time variance of the EOFs (ECs) $a_i = D \times E_i$ (the projection of D onto i^{th} EOF).
7. Reconstruct the denoised data matrix by $D_c = \sum_{i=1}^{q} a_i(E_i)$, $q < n$. Denoised version of S, S_c can be computed using D_c and the mean value of each columns of S.

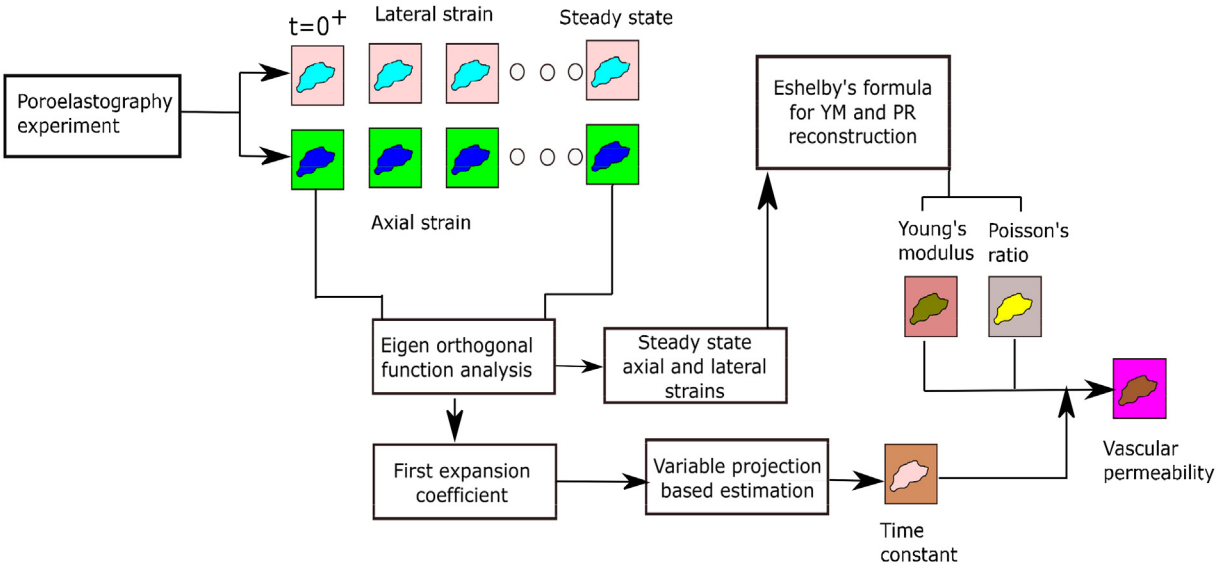

Fig. 3. Block diagram of the proposed technique.

normal tissue is estimated using the following formula [28]

$$L_p = \frac{1}{\tau}\frac{1}{H_A \frac{S}{V}}. \tag{12}$$

The block diagram for the proposed technique showing each step is shown in Fig. 3.

5. Simulations

5.1. FE simulations

A commercial FE simulation software namely ABAQUS, Abaqus Inc, Providence, RI, USA was used to create the displacements and strains of poroelastic samples used in this study under boundary conditions mimicking the real ultrasound elastography experiments. An 'effective stress' principle is used in ABAQUS [16], where the total applied stress is assumed to be sum of the fluid stress and the elastic or effective stress.

The samples considered in our FE simulations are of cylindrical shape with a spherical inclusion (Fig. 1). Because of the symmetry of the sample and the inclusion, the solution plane for the sample can be considered as 2D shown in Fig. 4. The samples were compressed from top and the bottom side was kept static.

The poroelastic samples were modeled as linearly elastic, isotropic, incompressible, permeable solid phases saturated with an incompressible fluid. For each sample, a single 2D solution plane (shown in Fig. 4) was analyzed in ABAQUS. The mesh element type used for this analysis was CAX4RP and there were 81,799 elements in the solution plane. The dimension of the solution plane for all the simulated samples is 20 mm in width and 40 mm in height. The radius of the inclusion was

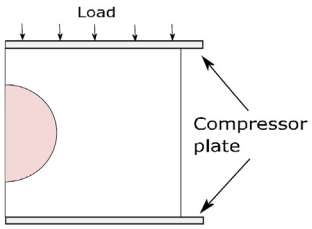

Fig. 4. The 2D solution plane for the three dimensional sample. The sample is compressed between two compressor plates. The compression is applied along the y direction.

7.5 mm. The zero fluid pressure boundary conditions on the right hand side of the samples were imposed to ensure the flow of the fluid only in the right direction.

An instantaneous stress of 1 kPa was applied for creep experiment simulation. The total analysis was recorded for 60 s in each step of 0.1 s. The readers are referred to Refs. [22,23] for detail of the poroelastic simulation in ABAQUS.

The mechanical properties of the samples used in our simulations were chosen following [30,38]. In all cases, the Poisson's ratio was assumed to be 0.49 in the background (normal) tissue and 0.4/0.47 in the inclusion (tumor) [30]. The Young's moduli of the tumor and normal tissue were assumed to be 97.02/163.90 and 32.78 kPa [30]. $\frac{S}{V}$ has been chosen as 20,000 m^{-1} for both the tumor and normal tissue following [29] for simulation cases. The description of the mechanical properties of the poroelastic samples (samples A, B and C) used in this study are shown in Table 2. In Table 2, subscripts i denotes the inclusion and b denotes the background. The true axial/lateral strain TC for

Table 2
Description of the poroelastic samples.

Sample	E_i (kPa)	ν_i	$L_{p,i}$ (m(Pa s)$^{-1}$)	k_i ($m^4N^{-1}s^{-1}$)	E_b (kPa)	ν_b	$L_{p,b}$ (m(Pa s)$^{-1}$)	k_b (m$m^4N^{-1}s^{-1}$)	τ_i (s)	τ_b (s)
A	97.02	0.47	2.83×10^{-11}	3.1×10^{-14}	32.78	0.49	9.45×10^{-12}	6.4×10^{-15}	3.03	9.43
B	97.02	0.40	8.35×10^{-11}	3.1×10^{-14}	32.78	0.49	9.45×10^{-12}	6.4×10^{-15}	2.88	9.43
C	163.90	0.40	2.83×10^{-11}	3.1×10^{-14}	32.78	0.49	9.45×10^{-12}	6.4×10^{-15}	5.04	9.43

sample A, B and C inside the inclusion are 3.03, 2.88, 5.04 s and in the background region is 9.43 s for all the samples shown in Table 2. These values of strain TC have been computed following [30].

5.2. Ultrasound simulations

The simulated pre- and post-compression temporal ultrasound radio frequency (RF) data were generated from the mechanical displacements obtained from FE simulation using a convolution model [10]. Bilinear interpolation was performed on the input mechanical displacement data prior to the computation of the simulated RF frames [7]. The simulated ultrasound transducer had 128 elements, frequency bandwidth between 5 − 14 MHz, a 6.6 MHz center frequency, and 50% fractional bandwidth at − 6 dB. The transducer's beamwidth was assumed to be dependent on the wavelength and to be approximately 1 mm at 6.6 MHz [44]. The sampling frequency was set at 40 MHz and Gaussian noise was added to set the SNR at 20, 30 or 50 dB. To compute the elastograms from the pre- and post-compressed RF data, we used the method described in Ref. [21].

An averaging filter of size 5 × 5 pixels is applied on all the estimates (YM, PR, TC, VP) of 128 × 128 pixels from ultrasound simulation.

5.3. Parameter setting in different methods

We compare the performance of the proposed method with that of a Kalman filter, which is often used and has been found to be more effective in removing noise from axial and lateral strains than other available techniques [21,45]. In the Kalman filter, the window length along axial direction is chosen as 43 and along lateral direction as 13 [45]. Variable projection method is used for curve fitting on the axial strain/first EC from EOF analysis to estimate the TC [41]. To compare the performance of Kalman filter and the proposed method in estimating strain TC from FE and ultrasound simulation data at different noise levels, the initial guess is set to 0.1 times of the true value in the variable projection method. In case of in vivo experiment data, the initial guess is set to 10 s in the variable projection technique.

5.4. Image quality analysis of simulation results

Image quality of YM, PR and VP images was quantified using PRE (percent relative error). The PRE is defined as

$$\text{PRE} = \frac{\rho_e - \rho_t}{\rho_t} \times 100, \tag{13}$$

where ρ_e is the mean estimated parameter i.e., YM, PR or VP of the inclusion and ρ_t is its true parameter shown in Table 2.

6. Experiments

We performed in vivo experiments on two mice with triple negative breast cancer, among which one is untreated and another is treated with Liposomes loaded with Epirubicin and conjugated with Lox antibody on the particle surface [27]. The experimental protocol was approved by Houston Methodist Research Institute, Institutional Animal Care and Use Committee (ACUC-approved protocol # AUP-0614-0033). We performed the elastography experiments using a 38-mm linear array transducer (Sonix RP, Ultrasonix, Richmond, BC, Canada) with a center frequency of 6.6 MHz and bandwidth of 5 − 14 MHz. An aqueous ultrasound gel pad (Aquaflex, Parker Laboratories, NJ, USA) was placed between the compressor plate and the animal. Creep experiments were performed on the anesthetized animals, where a constant compression was applied on the animal. A force sensor (Tekscan, Boston, MA, USA) was used to measure the applied compression. The ultrasound RF data acquisition was synchronized to the compression. We acquired data for up to 1 min with a sampling rate of 10 samples/second. The readers are referred to Ref. [27] for details on the in vivo experiments.

To estimate the YM and PR of the tumor and normal tissues, we used the method described in Ref. [27]. Accurate estimation of both axial and lateral strains is required to obtain accurate estimation of YM and PR using this method. We estimated the lateral and axial strains using the technique proposed in Islam et al. [21].

The surface area to volume ratio of the capillary walls ($\frac{S}{V}$) inside the tumor was computed using the following equation [51]

$$\frac{S}{V} = 10 f V_t^g, \tag{14}$$

where V_t is the volume of the tumor, which is computed as $V_t = \frac{4}{3}\pi l_1^2 l_2$, $f = 54.68$, $g = -0.2021$ [51]. Here, l_1 and l_2 are the lengths of lateral and axial semi-axis of elliptic tumor in units of mm and $\frac{S}{V}$ is in units of cm^{-1}. For spherical shaped tumor, $l_1 = l_2$.

7. Results

7.1. FE simulations

Fig. 5 shows the results obtained from the FE simulations. Specifically, we show the reconstructed YM, PR, axial strain TC and VP obtained from the strain data provided by the FEM, with no ultrasound involvement, for sample A. These YM, PR, and VP images match the

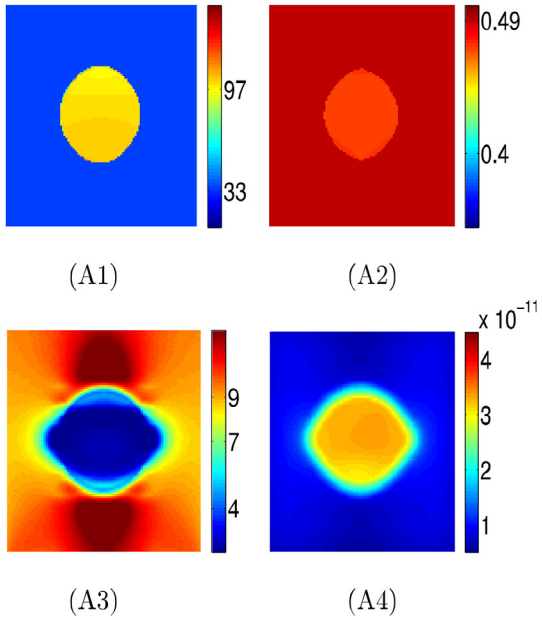

Fig. 5. Reconstructed YM (kPa), PR, strain TC (s) and VP (m(Pa s)$^{-1}$) from FEM strains are shown in A1-A4, respectively.

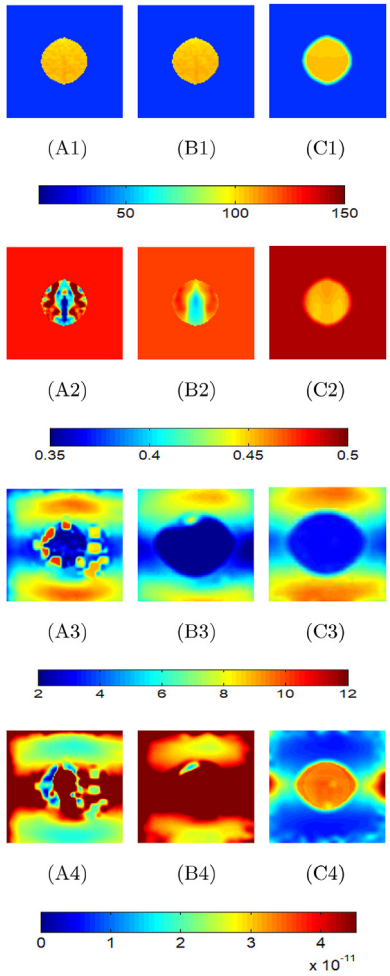

Fig. 6. Estimated parameters at 20 dB SNR by different techniques. (1) YM (2) PR (3) TC (4) VP from (A) noisy strains (B) Kalman filtered strains (C) EOF denoised strains. The units of YM, TC and VP are kPa, s and m(Pa s)$^{-1}$.

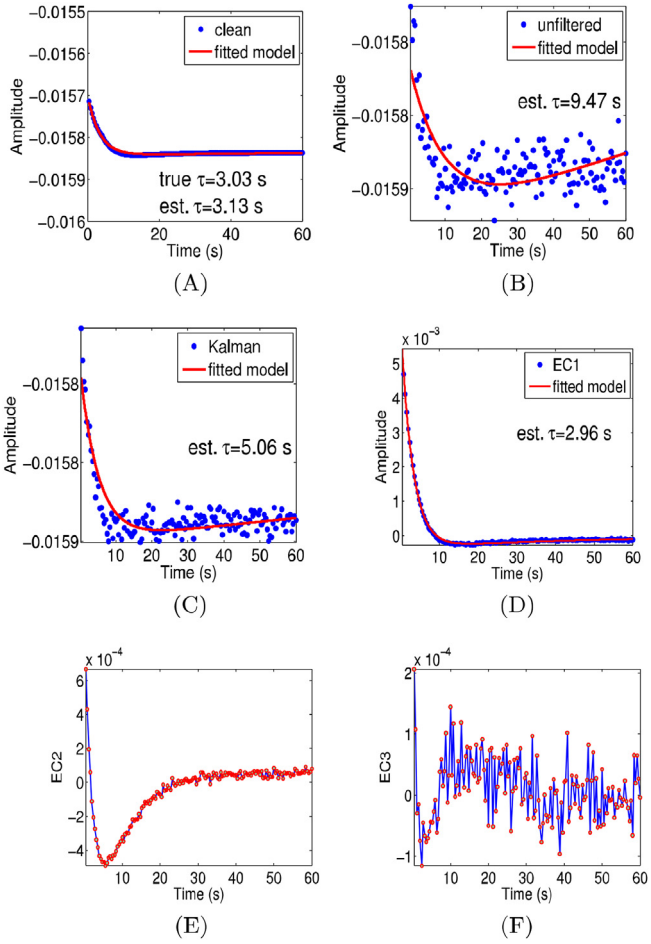

Fig. 7. Fitted curve on (A) clean axial strain (B) unfiltered axial strain at 20 dB SNR (C) Kalman filtered axial strain and (D) first EC. Second and third ECs are shown in (E) and (F).

true mechanical parameters given as input to the finite element simulation software (Table 2). From (A3, A4), we see that although the tumor is of spherical shape, the estimated axial strain TC and VP are elliptic in shape. The reason behind this is the fluid flow toward two side boundaries of the sample, which influences the dynamic strains at the regions between the inclusion boundary to the side boundaries and as such the estimated TCs in this region.

7.2. Ultrasound simulations

Axial strain TC, VP elastograms along with the YM and PR estimated from unfiltered and Kalman filtered strains and strains from EOF analysis are shown in Fig. 6 for 20 dB SNR for sample A. From Fig. 6 (A1, B1), we see that the reconstructed YM has values larger than the true value in case of unfiltered and Kalman filtered strains. The reconstructed YM from EOF analysis denoised strains has values close to the true value (C1). As the estimation of lateral component of strain is noisier than the axial component, the reconstructed PR from the unfiltered and Kalman filtered strains are noisier and has values much deviated from the true value in comparison to the YM values (A2, B2). However, the reconstructed PR from EOF analysis denoised strains shown in Fig. 6 (C2) is smooth and clearly similar to the true PR image (Fig. 5 A2).

The curve fitting technique fails to provide any sensible estimate in many pixels in the axial strain TC image because of high noise in case of unfiltered strain data as seen in Fig. 6 (A3). Although in case of Kalman filtered strain, the estimator can estimate the strain TC, the TC estimates at many places are incorrect (B3). On the other hand, the axial strain TC estimated from the first EC (C3) is smooth and have values that match with the strain TC computed from input mechanical properties.

The estimated VP images from unfiltered and Kalman filtered strains have very low similarity with the true VP maps (Fig. 6 (A4, B4)). At many points, the values are incorrect. The VP image estimated from EOF analysis is smooth and has values close to the true VP in both the inclusion and background (Fig. 6 (C4)). We note that, due to reduced accuracy in the axial and lateral displacement and strain estimations at the edges of the elastograms, the reconstructed VP images are more affected by noise at the edges than in other parts of the image.

The reconstructed YM and PR from axial strain elastogram by EOF analysis in Fig. 6 is based on the first EC only, and other ECs have been discarded. The axial strain TC is estimated from the first EC and VP depends on the strain TC, YM and PR. In Fig. 7, we show a temporal curve at a single pixel inside the inclusion of clean, unfiltered and Kalman filtered axial strains and temporal curves of first, second and third ECs in EOF analysis for sample A at 20 dB SNR. We also show the fitted exponential curves associated with them. We see, from (B) and (C), that the curves corresponding to unfiltered and Kalman filtered strains are noisy and the estimated TCs from the fitted curves are incorrect. In case of the clean strain (A) and first EC (D), we see that the estimator could fit the curves appropriately and estimated TCs are close to the actual value of TC.

Several important observations can be made from Fig. 7. First of all,

Table 3
PRE (%) in estimated YM, PR and VP of inclusions in poroelastic samples by different methods in creep experiments at SNRs of 20,30 and 50 dB.

SNR (dB)		Sample A			Sample B			Sample C		
		YM	PR	VP	YM	PR	VP	YM	PR	VP
20	Noisy	8.34	6.42	153.39	8.32	7.12	129.85	10.22	10.02	148.22
	Kalman	7.59	5.15	84.16	7.34	5.99	77.10	8.65	8.12	87.03
	EOF	3.27	3.10	14.22	4.34	2.42	14.19	5.14	3.11	13.77
30	Noisy	8.25	6.16	130.75	8.21	6.91	110.43	9.59	9.71	123.03
	Kalman	7.46	4.79	80.69	6.58	5.64	72.39	8.12	7.55	58.11
	EOF	3.05	2.84	12.71	3.74	1.83	13.12	4.34	3.04	11.39
50	Noisy	8.19	6.08	64.70	8.14	6.03	51.09	9.33	8.53	71.54
	Kalman	7.42	4.58	32.70	5.98	4.21	43.03	7.65	7.12	41.12
	EOF	3.01	2.59	9.46	3.12	1.38	10.17	2.97	1.81	10.73

although the unfiltered axial strain (B) is extremely noisy, the first EC (D) has a clear exponential profile. Other ECs (E, F) are noisy and larger effect of noise on these ECs can be clearly seen. Secondly, the magnitude of the first EC is larger than that of the second EC by almost 10 times and than that of the third EC by almost 25 times. This proves than the first EC contains most of the signal variance. Finally, although the axial strain has a small dynamic range (− 0.0157 − −0.01587) compared to the maximum amplitude (− 0.01587), the first EC has large dynamic range (0.005 − 0) compared to its maximum amplitude (0.005), which is useful in estimation of TC by curve fitting techniques.

Table 3 shows the PRE computed inside the inclusion from the YM, PR and VP images obtained by different methods at SNR levels of 20, 30 and 50 dB. From this table, we see that the PRE decreases with increment of SNR levels for all the methods in all the parameters. The PRE values in estimated YM, PR and VP in case of sample A are 8.34, 6.42 and 153.39% at SNR of 20 dB for unfiltered data, which reduce to 8.19, 6.08 and 64.70% at SNR of 50 dB. On the other hand, at the SNR of 20 dB, in case of Kalman filtered data, the PRE values in estimated YM, PR and VP for sample A are 7.59, 5.15 and 84.16%, which reduce to 7.42, 4.58 and 32.70% at 50 dB SNR. For the EOF analyzed data, PRE values in estimated YM, PR and VP in case of sample A are 3.27, 3.10 and 14.22% at SNR of 20 dB, which reduce to 3.01, 2.59 and 9.46% at SNR of 50 dB. Similar trend in PRE for other samples (B and C) can be seen at different SNR levels in Table 3. The PRE increases in estimated YM in sample C because of high YM contrast between inclusion and background, and the PRE increases in estimated PR in sample B and C in comparison to sample A because of high PR contrast.

7.3. Experiments

The estimated YM, PR and VP elastograms along with the B-mode images at three time points for the untreated tumor has been shown in Fig. 8. The increment of the tumor size from week 1 to week 2 can be clearly appreciable from the B-mode images. From Fig. 8, we see that the YM increases with time in this tumor from first to third week. The YM of this tumor is around 50 kPa at the first week, which increases to 75 kPa at second week and then to more than 90 kPa at third week. The PR is higher in first week for this tumor, which has similar values in second and third week. The VP image for this tumor has very small value (close to 1×10^{-11} m(Pas)$^{-1}$) at the first week, which increases by at least 3 times in second week and 6 times in third week in most pixels inside the tumor.

The estimated YM, PR and VP elastograms along with the B-mode images for the treated tumor at three weeks are shown in Fig. 9. From the B-mode images, we see that the tumor remains almost same in size in all three weeks. The increment of YM is much smaller than the untreated one from first to third week. Such arrest of size and stiffness is preferably because of the treatment administration. The PR remains almost same in all three weeks as seen in (A3, B3, C3). The VP images are shown in (A4, B4, C4). The VP value inside this tumor is close to 8×10^{-11} m(Pas)$^{-1}$ in the first week, which reduces to around 4×10^{-11} m(Pas)$^{-1}$ in second week and then to 1×10^{-11} m(Pas)$^{-1}$ in the third week. The reduction of VP may be because of the application of treatment. This observation correlates with the observation that the VP decreases with treatment administration from the literature [29].

The mean values of YM, PR and VP in the treated and untreated tumors are shown in Table 4. From this table, the fast increment of YM and VP can be clearly seen in the untreated tumor, where the YM increases slowly in the treated tumor and the VP decreases with time. The PR values are almost same in treated and untreated tumors in all three weeks. However, overall, the PR is higher in the treated tumor than the untreated one.

8. Discussion

In this paper, we proposed the use of EOF analysis to image the YM, PR and VP of cancers from noisy ultrasound poroelastography data. We reconstructed the steady state axial and lateral strains from noisy data using the first EC from EOF analysis and use these strains to estimate the YM and PR. For estimating the TC of axial strain, which is required to assess VP, we used curve fitting on the first EC, which is significantly less noisy and has larger dynamic range than the original strain signal.

YM is a parameter that is often used for determining cancer stage. PR is another important mechanical parameter, which has been found to be useful in cancer-related diseases such as lymphedema [3,43]. Accurate estimates of YM and PR are required for correct estimation of other important mechanical parameters such as VP. Estimation of VP is also important for diagnosis, prognosis and treatment of cancers as it can be an effective diagnostic marker and can provide useful information for drug delivery therapies and assessment of a number of treatments [29,38].

The proposed EOF analysis is an effective method for estimating the YM, PR and VP from noisy poroelastography strains and has several advantages over other filtering methods. Firstly, the first EC from EOF analysis has much larger dynamic range than the original noisy axial strain signal, which allows estimation of axial strain TC more accurately. Secondly, it is possible to efficiently control the amount of noise reduction in EOF analysis (see Fig. 7 (D-F)). As with noise removal we typically also lose some parts of the signals spectrum, it is important to know the amount of noise and amount of signal present in the decomposed parts of the noisy signal. In other filtering techniques such as Kalman, controlling the removal of amount of noise and signal is much harder, as these techniques do not decompose noisy signal in different parts.

In the literature, EOF analysis is also named as principal component analysis [4]. Application of EOF or principal component analysis in different fields is not new [39,40]. However, application of EOF analysis in poroelastography is novel. Based on our results, this method is an effective signal processing tool that can improve estimation of mechanical parameters from poroelastography experimental data.

One limitation of the VP estimation technique used in this paper is the assumption that VP is dominant over IP inside the tumor and

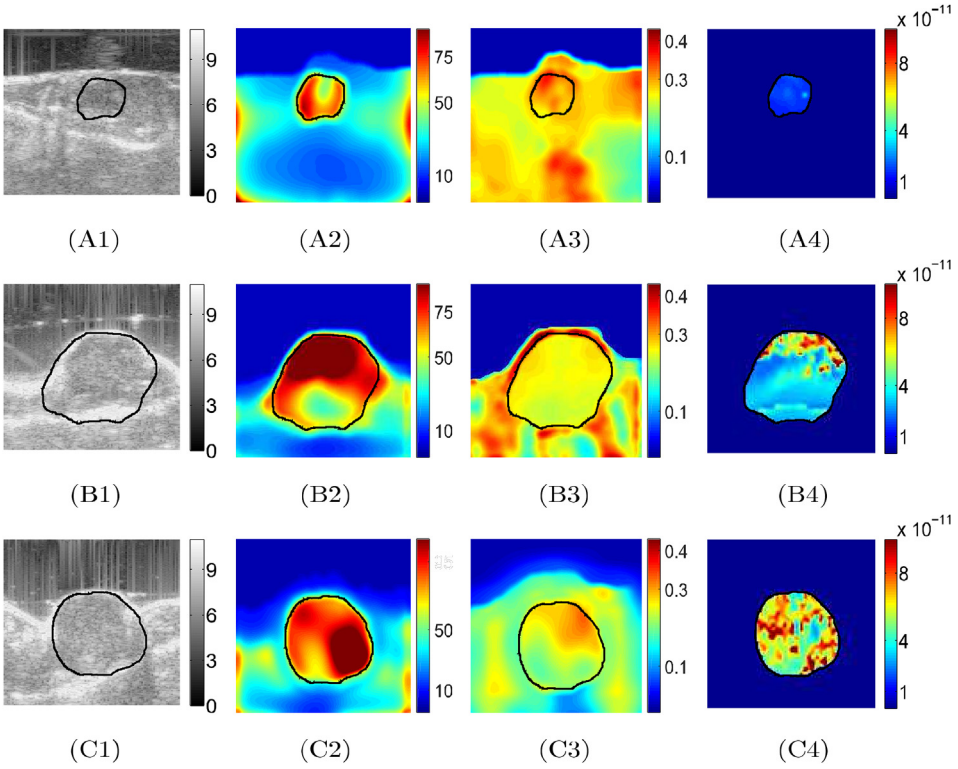

Fig. 8. Ultrasound B-mode images of an untreated tumor at three time points (week 1, week 2 and week 3) are shown in A1, B1 and C1, respectively. YM images (in kPa) at these time points are shown in A2, B2 and C2. PR images inside the tumor of the same mouse at three time points (week 1, week 2 and week 3) are shown in A3, B3 and C3, respectively. VP images (in m $(Pa\ s)^{-1}$) of the same tumor at three time points (week 1, week 2 and week 3) are shown in A4, B4 and C4, respectively. The YM and VP values in this tumor are seen increasing in consecutive weeks. In the first week, the YM is around 50 kPa which increases to around 75 kPa in second week and more than 90 kPa in the third week. The VP increases by almost 6 times from first to third week.

normal tissue [28]. In such case, during a poroelastography experiment, most of the fluid flows through the capillary walls because of the applied compression. Therefore, VP and axial strain TC do not depend on the geometry of the sample/inclusion [23,24]. In most available literature, VP is assumed to be much larger than IP in tumors [1,2,38,48]. Thus, this assumption should hold in tumors in most practical cases. This assumption may not be suitable to normal tissues. In some literature, IP and VP have been found to be of comparable values and, in some cases, IP was found to be dominant over VP in normal tissues [29]. In these cases, an analytical model of the strains would be necessary to consider the effects of VP, IP and the geometry of the inclusion/sample. Such model is not currently available. Since the underlying assumption that VP is much higher than IP (required by our method) may not be satisfied in the normal tissue region, we did not

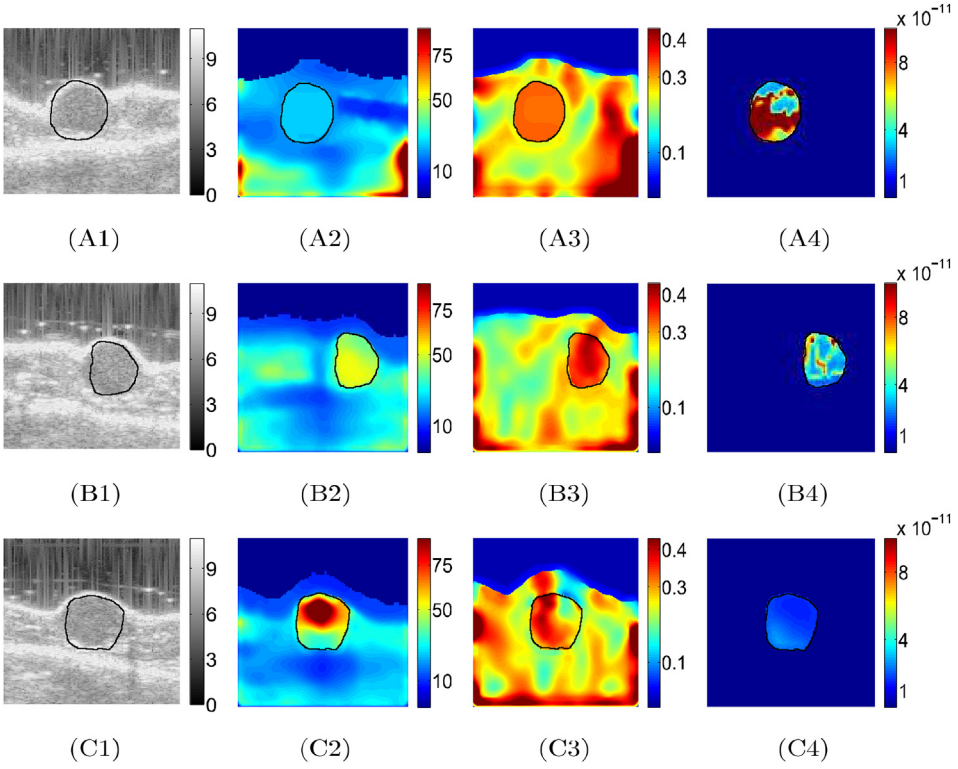

Fig. 9. Ultrasound B-mode images of a treated tumor at three time points (week 1, week 2 and week 3) are shown in A1, B1 and C1, respectively. YM images (in kPa) at these time points are shown in A2, B2 and C2. PR images inside the tumor of the same mouse at three time points (week 1, week 2 and week 3) are shown in A3, B3 and C3, respectively. VP images (in m $(Pa\ s)^{-1}$) of the same tumor at three time points (week 1, week 2 and week 3) are shown in A4, B4 and C4, respectively. The YM for this tumor is seen slightly increasing from first to second and then second to third week. However, VP in this tumor is seen decreasing in consecutive weeks. In the first week, the VP is more than 8×10^{-11} $m(Pas)^{-1}$ in many places inside the tumor, which decreases by more than 6 times in the third week.

Table 4
Mean and standard deviations of estimated YM, PR and VP in treated and untreated tumors at different time points. 'UT' refers to the untreated tumor and 'TT' refers to the treated tumor.

Sample	YM (kPa)			PR			VP (m(Pa s)$^{-1}$)		
	Week 1	Week 2	Week 3	Week 1	Week 2	Week 3	Week 1	Week 2	Week 3
UT	63.54 ± 7.19	77.61 ± 10.27	128.01 ± 31.20	0.29 ± 0.03	0.25 ± 0.03	0.24 ± 0.04	$4.31\times 10^{-13} \pm 1.12\times 10^{-13}$	$7.89\times 10^{-13} \pm 2.12\times 10^{-13}$	$1.45\times 10^{-12} \pm 3.92\times 10^{-13}$
TT	24.25 ± 2.14	29.22 ± 5.19	42.16 ± 8.19	0.31 ± 0.04	0.37 ± 0.03	0.37 ± 0.03	$5.66\times 10^{-11} \pm 8.14\times 10^{-12}$	$3.52\times 10^{-11} \pm 7.76\times 10^{-12}$	$1.68\times 10^{-11} \pm 3.19\times 10^{-12}$

show VP in normal tissue regions in our in vivo experimental results.

Currently, there are a number of invasive and non-invasive techniques to estimate the VP. Magnetic resonance imaging (MRI) modalities [8,11,31,46] and intravital microscopy (IVM) [34] are possible methods for VP estimation, but they are expensive, require specialized sample preparation and are computationally intense. The use of ultrasound methods to VP assessment would provide significant advantages over MRI and IVM.

In the present study, theory and algorithms to estimate VP were validated using simulations. A limited number of experimental datasets (six datasets-two untreated and treated mice at three timepoints) were used to demonstrate the feasibility of the proposed technique in vivo. In our results, VP increased consistently in the untreated tumors, whereas it decreased in the treated ones with time. These observations match well with those reported in the literature [5,6,29]. A limitation of the proposed study is the higher computation in reconstructing the YM, PR and VP. The present configuration of EOF analysis requires 0.17 s on average in an Intel Xeon 3.5 GHz PC with 32 GB RAM for each pixel in the axial and lateral strains (with axial and lateral strain data from FE simulation for the computational setup described in the simulations section).

9. Conclusion

EOF analysis has been used in this paper to determine the mechanical parameters of a tumor embedded in normal tissue from noisy porelastography data. The efficacy of the proposed methodology has been proved through finite element and ultrasound simulations. In vivo feasibility was also demonstrated. Based on the superior performance of the proposed method in comparison to techniques commonly used to denoise elastography data, the proposed method may have a positive impact on clinical applications of poroelastography.

Conflict of interest statement

None declared.

Acknowledgments

This work was funded in part by the U.S. Department of Defense under grant W81XWH- 18-1-0544 (BC171600).

References

[1] L.T. Baxter, R.K. Jain, Transport of fluid and macromolecules in tumors. i. role of interstitial pressure and convection, Microvasc. Res. 37 (1) (1989) 77–104.
[2] L.T. Baxter, R.K. Jain, Transport of fluid and macromolecules in tumors. ii. role of heterogeneous perfusion and lymphatics, Microvasc. Res. 40 (2) (1990) 246–263.
[3] G.P. Berry, J.C. Bamber, P.S. Mortimer, N.L. Bush, N.R. Miller, P.E. Barbone, The spatio-temporal strain response of oedematous and nonoedematous tissue to sustained compression in vivo, Ultrasound Med. Biol. 34 (4) (2008) 617–629.
[4] H. Björnsson, S. Venegas, A manual for eof and svd analyses of climatic data, CCGCR Report 97 (1) (1997) 112–134.
[5] F. Chammings, H. Latorre-Ossa, M. Le Frère-Belda, V. Fitoussi, T. Quibel, F. Assayag, E. Marangoni, G. Autret, D. Balvay, L. Pidial, et al., Shear wave elastography of tumour growth in a human breast cancer model with pathological correlation, Eur. Radiol. 23 (8) (2013) 2079–2086.
[6] F. Chammings, M.-A. Le-Frre-Belda, H. Latorre-Ossa, V. Fitoussi, A. Redheuil, F. Assayag, L. Pidial, J.-L. Gennisson, M. Tanter, C.-A. Cunod, et al., Supersonic shear wave elastography of response to anti-cancer therapy in a xenograft tumor model, Ultrasound Med. Biol. 42 (4) (2016) 924930.
[7] A. Chaudhry, Effect of Boundary Conditions on Performance of Poroelastographic Imaging Techniques in Non Homogeneous Poroelastic Media, Master's thesis Texas A&M University, 2010.
[8] H. Chen, X. Tong, L. Lang, O. Jacobson, B.C. Yung, X. Yang, R. Bai, D.O. Kiesewetter, Y. Ma, H. Wu, et al., Quantification of tumor vascular permeability and blood volume by positron emission tomography, Theranostics 7 (9) (2017) 2363.
[9] H. Chen, T. Varghese, Principal component analysis of shear strain effects, Ultrasonics 49 (4–5) (2009) 472–483.
[10] R.R. Desai, T.A. Krouskop, R. Righetti, Elastography using harmonic ultrasonic imaging: a feasibility study, Ultrason. Imag. 32 (2) (2010) 103–117.
[11] R. Elmghirbi, T.N. Nagaraja, S.L. Brown, K.A. Keenan, S. Panda, G. Cabral, H. Bagher-Ebadian, G.W. Divine, I.Y. Lee, J.R. Ewing, Toward a noninvasive estimate of interstitial fluid pressure by dynamic contrast-enhanced mri in a rat model of cerebral tumor, Magn. Reson. Med. (2018).
[12] J.D. Eshelby, The determination of the elastic field of an ellipsoidal inclusion, and related problems, Proceedings of the Royal Society of London A: Mathematical, Physical and Engineering Sciences, vol. 241, The Royal Society, 1957, pp. 376–396.
[13] A. Fukuoka, The central meteorological observatory, a study on 10-day forecast (a synthetic report), Geophys. Mag. 22 (3) (1951) 177–208.
[14] G. Golub, V. Pereyra, Separable nonlinear least squares: the variable projection method and its applications, Inverse Probl. 19 (2) (2003) R1.
[15] A. Hannachi, I. Jolliffe, D. Stephenson, Empirical orthogonal functions and related techniques in atmospheric science: a review, Int. J. Climatol.: J. R. Meteorol. Soc. 27 (9) (2007) 1119–1152.
[16] K. Hibbitt, Sorensen, Inc. Abaqus/explicit User's Manual, (2005) version 6.5. 1.
[17] Z. Hu, H. Zhang, J. Yuan, M. Lu, S. Chen, H. Liu, An h strategy for strain estimation in ultrasound elastography using biomechanical modeling constraint, PLoS One 8 (9) (2013) e73093.
[18] M.A. Hussain, S.K. Alam, S.Y. Lee, M.K. Hasan, Robust strain-estimation algorithm using combined radiofrequency and envelope cross-correlation with diffusion filtering, Ultrason. Imag. 34 (2) (2012) 93–109.
[19] M.T. Islam, A. Chaudhry, R. Righetti, A robust method to estimate the time constant of elastographic parameters, IEEE Trans. Med. Imag. 38 (6) (June 2019) 1358–1370, https://doi.org/10.1109/TMI.2019.2894782.
[20] M.T. Islam, A. Chaudhry, R. Righetti, An Analysis of the Error Associated to Single and Double Exponential Approximations of Theoretical Poroelastic Models, (2019) In press, Ultrasonic Imaging.
[21] M.T. Islam, A. Chaudhry, R. Righetti, An analysis of the error associated to single and double exponential approximations of theoretical poroelastic models, Ultrasonic Imag. 41 (2) (2019) 94–114.
[22] M.T. Islam, A. Chaudhry, G. Unnikrishnan, J. Reddy, R. Righetti, An analytical poroelastic model for ultrasound elastography imaging of tumors, Phys. Med. Biol. 63 (2) (2018) 025031.
[23] M.T. Islam, J. Reddy, R. Righetti, An analytical poroelastic model of a non-homogeneous medium under creep compression for ultrasound poroelastography applicationspart i, J. Biomech. Eng. 141 (6) (2019) 060902.
[24] M.T. Islam, J. Reddy, R. Righetti, An analytical poroelastic model of a non-homogeneous medium under creep compression for ultrasound poroelastography applicationspart ii, J. Biomech. Eng. 141 (6) (2019) 060903.
[25] M.T. Islam, R. Righetti, A Novel Filter for Accurate Estimation of Fluid Pressure and Fluid Velocity Using Poroelastography. Computers in Biology and Medicine, (2018).
[26] M.T. Islam, R. Righetti, An analytical poroelastic model of a spherical tumor embedded in normal tissue under creep compression, J. Biomech. 89 (2019) 48–56.
[27] M.T. Islam, S. Tang, C. Liverani, E. Tasciotti, R. Righetti, Non-invasive Imaging of the Young's Modulus and Poisson's Ratio of Cancer Tumor in Vivo, (2018) arXiv preprint arXiv:1809.02929.
[28] M.T. Islam, E. Tasciotti, R. Righetti, Estimation of Vascular Permeability in Irregularly Shaped Cancers Using Ultrasound Poroelastography. Under Review, IEEE Transactions on Biomedical Engineering, 2018.
[29] R.K. Jain, R.T. Tong, L.L. Munn, Effect of vascular normalization by antiangiogenic therapy on interstitial hypertension, peritumor edema, and lymphatic metastasis: insights from a mathematical model, Cancer Res. 67 (6) (2007) 2729–2735.
[30] R. Leiderman, P.E. Barbone, A.A. Oberai, J.C. Bamber, Coupling between elastic strain and interstitial fluid flow: ramifications for poroelastic imaging, Phys. Med. Biol. 51 (24) (2006) 6291.
[31] L.J. Liu, S.L. Brown, J.R. Ewing, B.D. Ala, K.M. Schneider, M. Schlesinger,

Estimation of tumor interstitial fluid pressure (tifp) noninvasively, PLoS One 11 (7) (2016) e0140892.
[32] M. Lu, D. Wu, W.-h. Lin, W. Li, H. Zhang, W. Huang, A stochastic filtering approach to recover strain images from quasi-static ultrasound elastography, Biomed. Eng. Online 13 (1) (2014) 15.
[33] F.W. Mauldin Jr., H.T. Zhu, R.H. Behler, T.C. Nichols, C.M. Gallippi, Robust principal component analysis and clustering methods for automated classification of tissue response to arfi excitation, Ultrasound Med. Biol. 34 (2) (2008) 309–325.
[34] E.F. Meijer, J.W. Baish, T.P. Padera, D. Fukumura, Measuring vascular permeability in vivo, The Tumor Microenvironment, Springer, 2016, pp. 71–85.
[35] T. Mura, Micromechanics of Defects in Solids. Mechanics of Elastic and Inelastic Solids, second, revised edition, Martinus Nijhoff Publishers, Dordrecht, The Netherlands, 1987.
[36] R. Muthupillai, R.L. Ehman, Magnetic resonance elastography, Nat. Med. 2 (5) (1996) 601–603.
[37] S.P. Nair, X. Yang, T.A. Krouskop, R. Righetti, Performance analysis of a new real-time elastographic time constant estimator, IEEE Trans. Med. Imag. 30 (2) (2011) 497–511.
[38] P.A. Netti, L.T. Baxter, Y. Boucher, R. Skalak, R.K. Jain, Macro-and microscopic fluid transport in living tissues: application to solid tumors, AIChE J. 43 (3) (1997) 818–834.
[39] A. Obukhov, Statistically homogeneous fields on a sphere, Usp. Mat. Nauk 2 (2) (1947) 196–198.
[40] A. Obukhov, The statistically orthogonal expansion of empirical functions, Bull. Acad. Sci. USSR. Geophys. Ser. (English Transl.) 1 (1960) 288–291.
[41] D.P. Oleary, B.W. Rust, Variable projection for nonlinear least squares problems, Comput. Optim. Appl. 54 (3) (2013) 579–593.
[42] J. Ophir, S. Alam, B. Garra, F. Kallel, E. Konofagou, T. Krouskop, T. Varghese, Elastography: ultrasonic estimation and imaging of the elastic properties of tissues, Proc. IME H J. Eng. Med. 213 (3) (1999) 203–233.
[43] R. Righetti, B.S. Garra, L.M. Mobbs, C.M. Kraemer-Chant, J. Ophir, T.A. Krouskop, The feasibility of using poroelastographic techniques for distinguishing between normal and lymphedematous tissues in vivo, Phys. Med. Biol. 52 (21) (2007) 6525.
[44] R. Righetti, J. Ophir, S. Srinivasan, T.A. Krouskop, The feasibility of using elastography for imaging the Poisson's ratio in porous media, Ultrasound Med. Biol. 30 (2) (2004) 215–228.
[45] H. Rivaz, E.M. Boctor, M.A. Choti, G.D. Hager, Real-time regularized ultrasound elastography, IEEE Trans. Med. Imag. 30 (4) (2011) 928–945.
[46] H.C. Roberts, T.P. Roberts, R.C. Brasch, W.P. Dillon, Quantitative measurement of microvascular permeability in human brain tumors achieved using dynamic contrast-enhanced mr imaging: correlation with histologic grade, Am. J. Neuroradiol. 21 (5) (2000) 891–899.
[47] F. Sebag, J. Vaillant-Lombard, J. Berbis, V. Griset, J. Henry, P. Petit, C. Oliver, Shear wave elastography: a new ultrasound imaging mode for the differential diagnosis of benign and malignant thyroid nodules, J. Clin. Endocrinol. Metab. 95 (12) (2010) 5281–5288.
[48] M. Soltani, P. Chen, Numerical modeling of interstitial fluid flow coupled with blood flow through a remodeled solid tumor microvascular network, PLoS One 8 (6) (2013) e67025.
[49] M. Tyagi, Y. Wang, T.J. Hall, P.E. Barbone, A.A. Oberai, Improving three-dimensional mechanical imaging of breast lesions with principal component analysis, Medical physics 44 (8) (2017) 4194–4203.
[50] P. Wellman, R.D. Howe, E. Dalton, K.A. Kern, Breast Tissue Stiffness in Compression Is Correlated to Histological Diagnosis, Harvard BioRobotics Laboratory Technical Report, 1999, pp. 1–15.
[51] W. Zhan, W. Gedroyc, X.Y. Xu, The effect of tumour size on drug transport and uptake in 3-d tumour models reconstructed from magnetic resonance images, PLoS One 12 (2) (2017) e0172276.